LANGMUIR Article
Cite This: Langmuir 2019, 35, 3404−3412
pubs.acs.org/Langmuir

Controlled Deposition of Nanosize and Microsize Particles by Spin-Casting

José Danglad-Flores,*[,†,‡] Karaneh Eftekhari,[‖] Andre G. Skirtach,[‖] and Hans Riegler*[,†]

[†]Max Planck Institute of Colloids and Interfaces, Theory and Bio-Systems, Science Park Golm, 14424 Potsdam, Germany
[‡]Technical University Berlin, Strasse des 17, Juni 135, 10623 Berlin, Germany
[‖]Department of Biotechology, Ghent University, 9000 Ghent, Belgium

Supporting Information

ABSTRACT: The deposition of nanosize and microsize spherical particles on planar solid substrates by hydrodynamic-evaporative spin-casting is studied. The particles are dispersed in a volatile liquid, which evaporates during the process, and the particles are finally deposited on the substrate. Their coverage, Γ, depends on the processing parameters (concentration by weight, particles size, etc.). The behavior of the particles during the spin-casting process and their final Γ values are investigated. It is found that for up to particle diameters of a few micrometers, particle deposition can be described by a theoretical approach developed for the spin-casting of polymer solutions (Karpitschka, S.; Weber, C. M.; Riegler, H. *Chem. Eng. Sci.* **2015**, *129*, 243−248. Danglad-Flores, J.; Eickelmann, S.; Riegler, H. *Chem. Eng. Sci.* **2018**, *179*, 257−264). For large particles, this basic theory fails. The causes of this failure are analyzed, and a corrected, more general theoretical approach is presented. It takes into account particle size effects as well as particle sedimentation. In summary, we present new insights into the spin-cast process of particle dispersions, analyze the contributions affecting the final particle coverage, and present a theoretical approach which describes and explains the experimental findings.

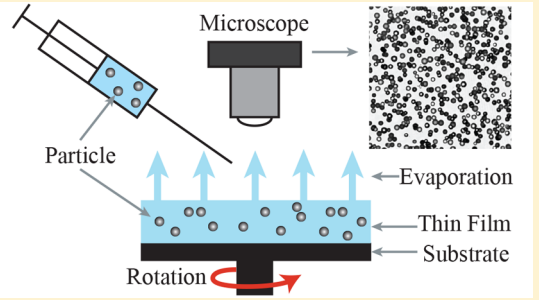

INTRODUCTION

Evaporative spin-casting (i.e., spin-casting of mixtures of volatile (solvent) and nonvolatile (solute) components) is a widely used process for fabricating thin coatings of a nonvolatile component on solid substrates. Until a few years ago, in most cases the nonvolatile solute was a polymer,[3] but recently the spin-casting of suspensions of nanosize objects, such as nanoparticles,[4] nanorods,[5] and nanowires,[6,7] in volatile liquids has also been used to produce thin layers of nanosize objects on solid substrates. Thus, for instance ordered monolayers[8−10] and multilayers[11,12] have been prepared with special optical properties.[5,13−15] The particle coverage is an important system parameter which is adjusted by the processing parameters (initial concentration, rotational speed, solvent, etc.). Until now, the processing conditions for obtaining a certain desired particle layer coverage from a certain particle/liquid dispersion were derived empirically by trial and error.[16] There was no consistent and reliable theoretical approach available which allows the prediction of particle deposition based on the applied processing parameters.

Recently, Karpitschka et al.,[1] based on experimental data and the earlier work of others,[17−23] provided a rather transparent and practically useful theoretical approach for the evaporative spin-casting of solutions with low solute concentrations. Their analysis gives insight into the solute enrichment and film formation process and allows quantitative predictions of the outcome of the spin-casting process based on the applied processing parameters. In essence, they identified the spin-casting process as a two-stage process. Upon deposition of the solution onto the rotating substrate, the liquid first flattens as a result of the competition between centripetal and viscous forces.[24] After a certain time, t_{tr} (transition time), which corresponds to a certain film thickness h_{tr} (transition height), film thinning starts to be dominated by evaporation. During this second stage, the solute gets enriched and finally forms a dry film on the substrate. Thus, t_{tr} and h_{tr}, which depend on spin-cast parameters E (evaporation rate) and ω (rotational speed), characterize the process and determine the result. Recently it has been shown[2] that with some substantial modification this scenario is valid even for solutions with rather high polymer concentrations. The resulting, easily applicable approach allows us to predict the final layer coverage (film thickness) for diluted molecular solutions of small molecules as well as for relatively highly concentrated polymer solutions leading to final film thicknesses of up to several micrometers.

In the following text, we extend this approach to dispersions of low and moderately high concentrations of particles in volatile liquids with particle sizes ranging from a few tens of nanometers to tens of micrometers. Spin-casting of particle dispersions differs from that of molecular solutions in at least two aspects:

Received: September 29, 2018
Revised: December 22, 2018
Published: January 23, 2019

(1) The size of the particles may reach or even exceed the thickness of the transition height (typically a few micrometers). Thus, even low particle concentrations may have an impact on the film-thinning behavior, hence the final coverage. (2) Sedimentation during the spin-casting process may contribute to the final coverage. In the following text, we will present experimental data with various types of particle dispersions, focusing on these questions. We will analyze the data in view of our earlier approach,[1,2] test its limits, and modify the approach to correctly predict the coverage in the case of particle dispersions.

Zeroth-Order Scenario for Hydrodynamic−Evaporative Film Thinning. The hydrodynamic−evaporative thinning of a Newtonian, volatile liquid film of thickness h on a rotating support is described by[1,17,24]

$$dh/dt = -2Kh^3 - E \quad (1)$$

Equation 1 assumes no slip at the liquid/substrate interface (lubrication approximation) and a free liquid surface. Contributions from surface tension and gravity are neglected. E is the evaporation rate. $K = \omega^2/(3\nu)$ describes the hydrodynamic behavior (ω = rotational speed, ν = kinematic viscosity). K and E are the two key parameters governing hydrodynamic−evaporative film thinning. For dilute solutions, in a zeroth-order approximation, K and E may be assumed to be constant during film thinning (i.e., the impact of solute enrichment (which occurs mainly in the late stages of the process) is neglected). It should also be noted that E depends on the rotational speed, ω.[2,17,22,25] K and E can be combined into a single parameter, namely h_{tr}, the transition height, which universally characterizes the hydrodynamic−evaporative spin-cast film-thinning process.[1] h_{tr} has an explicit physical meaning. It identifies the film thickness at the transition between film thinning dominated by hydrodynamics (in the early stages of the spin-cast process) and thinning dominated by evaporation (in the late stages of the process):

$$h_{tr} = (E/2K)^{1/3} \quad (2)$$

In the zeroth-order approximation, the total spin-cast time (from the liquid deposition to complete drying), t_{sc}, is a function only of K and E

$$t_{sc} = (2\pi/3^{3/2})(2E^2K)^{-1/3} \quad (3)$$

as well as the moment at which h_{tr} is reached, the transition time, t_{tr}:

$$t_{tr} \approx 1/2(2E^2K)^{-1/3} \approx 0.3t_{sc} \quad (4)$$

At the beginning of the spin-casting process, the solution is spreading and forming a thinning planar film driven by hydrodynamics. At this stage relative to the total amount of liquid evaporation, evaporative solute enrichment can be neglected. The solute concentration remains approximately c_0, the weighing in concentration. This is a reasonable assumption, as Karpitschka et al.[1] and Danglad-Flores et al.[2] have shown. Later, as soon as the film is thinner than h_{tr}, film thinning is due to evaporation only. Therefore, all of the solute, which is contained in the film with thickness h_{tr}, is finally deposited on the substrate:

$$\Gamma_0 \approx c_0 h_{tr} = c_0(E/2K)^{1/3} \quad (5)$$

Equation 5 can also be applied to particle dispersions, most conveniently by using c_0 in terms of particles per volume. Thus, the equation yields Γ_0 in number of particles per area. If the particle concentration is given as the mass fraction, x_0, then c_0 can be derived via $c_0 = x_0(3\rho_L)/(4\pi\rho_p R^3)$ (ρ_p, particle density; ρ_L, liquid density; and R, particle radius).

MATERIALS AND METHODS

Particles. Spherical silica particles (ρ = 2400 kg m^{-3}) with diameters of 50 and 200 nm (x_0 = 10%(w/w) in ethanol) and 1 μm (aqueous dispersion, x_0 = 5%(w/w)) were obtained from from Aldrich. Silica particles with a diameter of 550 nm (dry powder) were from Geltec. All silica particles had fairly uniform sizes (±10% in diameter).

Spherical gold nanoparticles with diameters of 400 nm in an aqueous dispersion ($c_0 \approx 1.9 \times 10^{14}$ particles/m^3) were purchased from Sigma-Aldrich.

Spherical calcium carbonate particles (vaterite, ρ = 1600 kg m^{-3}) were synthesized[26] in aqueous media, transferred to ethanol, decanted by centrifugation, and finally dried for storage. Their diameters varied considerably with a mean size of ∼2.6 μm. (For more info on the size distribution, see the Results and the Supporting Information.)

Spherical polystyrene particles (ρ = 1040 kg m^{-3}), with sizes of 0.52 and 1 μm (aqueous suspensions $x_0 \approx$ 1%(w/w)) were obtained from Duke Scientific; particles with diameters of 6, 8 (dry powder), and 25 μm (in aqueous suspension $x_0 \approx$ 1%(w/w)) were purchased from Thermo Scientific. The size distribution was fairly uniform (±10%).

Chemicals. Anhydrous ethanol (≥99.8%, max H_2O content 0.003%, ρ = 780 kg m^{-3}) used to prepare the particle dispersions was from VWR. A Milli-Q system provided the water (resistivity 18 MΩ cm). Ethanol (96.9%, VWR Chemistry and Chemicals), acetone (99.3%, J.T. Baker), sulfuric acid (96%, ROTH), hydrogen peroxide (30%, Merck), and water (Milli-Q) were used for the substrate surface cleaning/preparation.

Substrates. As substrates served ∼2 cm × 2 cm silicon wafer pieces with artificial oxide layers of (50 ± 1) nm thickness (Siegert Wafer) with an rms surface roughness of ∼0.5 nm.

Substrate Surface Preparation. The substrates were first cleaned in an ultrasonic bath by a sequence of immersions (for 10 min each) in (1) water, (2) ethanol, (3) acetone, (4) ethanol, and (5) water. In a second cleaning step, they were immersed in piranha solution (H_2O_2(35%)/H_2O(65%) and H_2SO_4(96%), 1:3 volume ratio) for 30 min. Finally, they were again immersed and sonicated for 10 min in water and stored therein. Just before use, they were dried by blowing with dry N_2 (purity 5.0).

Spin-Casting. Aliquots of ∼0.2 mL of the dispersions/suspension were deposited in the center of the substrate, which was already rotating at constant speed. A home-build spin-cast setup with the substrate exposed to the laboratory environment was used. (See also Figure 2.) To ensure a rather homogeneous particle distribution and reproducible x_0, the dispersions were sonicated right before the aliquot for the spin-cast deposition was taken.

Optical Online Observation of Film Thinning. An optical microscope (Axio Scope A1 from Zeiss, long working distance objectives, e.g., SLMPLN50× Olympus, NA = 0.35) with a homemade mechanical stand was used for the in situ observation of the spin-coating process from the top (Figure 2). As illumination light source served a blue diode laser (6 W, 445 nm, LDM-445-6000, Lasertack), despeckled by a combination of a liquid light guide and a rotating diffusor.[27] The spin-coater was mounted on an $X-Y$ table to enable variable observation spots. Optical imaging was improved by interference enhanced reflection[28] and image processing.[29] Imaging was performed with an EoSenseCL MC1362 high-speed camera (Mikrotron GmbH) of up to 1000 fps. The film-thinning behavior was derived by interferometry from the brightness variations during film thinning.[1,2,27,29,30] (See the Supporting Information for thinning curves of water and ethanol.)

Measurement of the Final Coverage. Except for the experiments with calcium carbonate, the final particle coverages Γ were determined by directly counting the number of particles per area by either AFM (diameters of 50−200 nm) or by optical microscopy (diameters of 500 nm and larger). The areas inspected by AFM were between

DOI: 10.1021/acs.langmuir.8b03311
Langmuir 2019, 35, 3404−3412

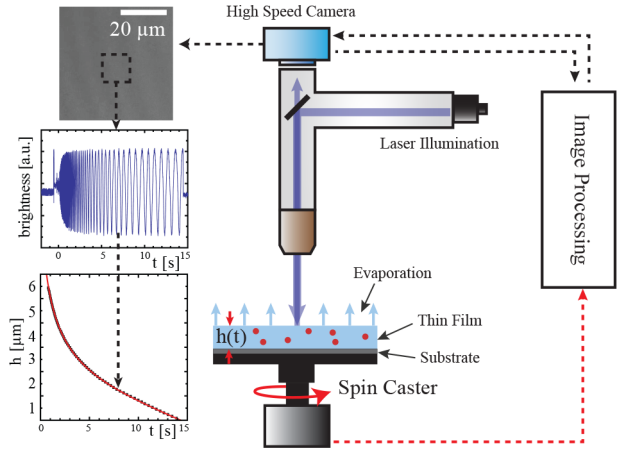

Figure 2. Experimental setup. The spin-caster is synchronized with the image recording/processing. The vertical sequence on the left (from the top: optical image → interference pattern → film thinning) indicates how online film thinning is derived from the optical images.

30 μm × 30 μm and 100 μm × 100 μm, and those inspected optically ranged between 200 μm × 200 μm and 2 mm × 2 mm (via an XIMEA-MQ042MG-CM high-resolution camera with FLN10× (NA = 0.25), SLMPLN50× (NA = 0.35), and SLMPLN100× (NA = 0.6) objectives from Olympus). The images were processed and analyzed by the ImageJ and Gwyddion software packages. In all cases, at least three different areas were investigated, including areas at the substrate center as well as at some distance from the center. It is found that within a radius 8 mm away from the center of the rotation the coverage does not change (Supporting Information). Care was taken to ensure that the data were representative of the samples.

RESULTS

Images of NP Coverage. Figure 3 shows examples of AFM and optical images with particles deposited on the silica surfaces. In all cases, the particle concentration was x_0 = 0.01 w/w dispersed in water. Therefore, the concentration in numbers of particles per volume decreases rapidly with the particle diameter, d_p. As a result, the coverage in number of particles per area also decreases with increasing particle size. Frames A–D present SiO_2 particles with diameters of 50, 200, 550, and 1000 nm. Frames E and F show PS particles with diameters of d_p= 8 and 25 μm. Image G shows the case of $CaCO_3$ particles with a mean diameter of $d_p \approx 2.6$ μm as derived from the size distributions by optical microscopy (frame H). One can see that in some cases the particles are not uniformly distributed on the surface. In particular, in the case of small diameters the particles tend to form 2D aggregates. Most pronounced is the particle aggregation in the case of the $CaCO_3$ particles. In the cases of the silica and the PS particles, the particles have rather uniform sizes and individual particles can be easily identified. Thus, it is possible to measure quite precisely the average particle coverage in number of particles per area just by counting the particles. With the calcium carbonate particles, the approach of counting particles per area is rather awkward because the particle size varies considerably. Therefore, we determined the relative amount of surface area which is covered by the particles. Separately we determined the particle size distribution by analyzing cases of low coverage from low weighing in concentration, which allowed us to discriminate individual particles (Supporting Information). From the combination of the size distribution and the surface coverage, we *estimated* the coverage of the entire sample in number of particles per area.

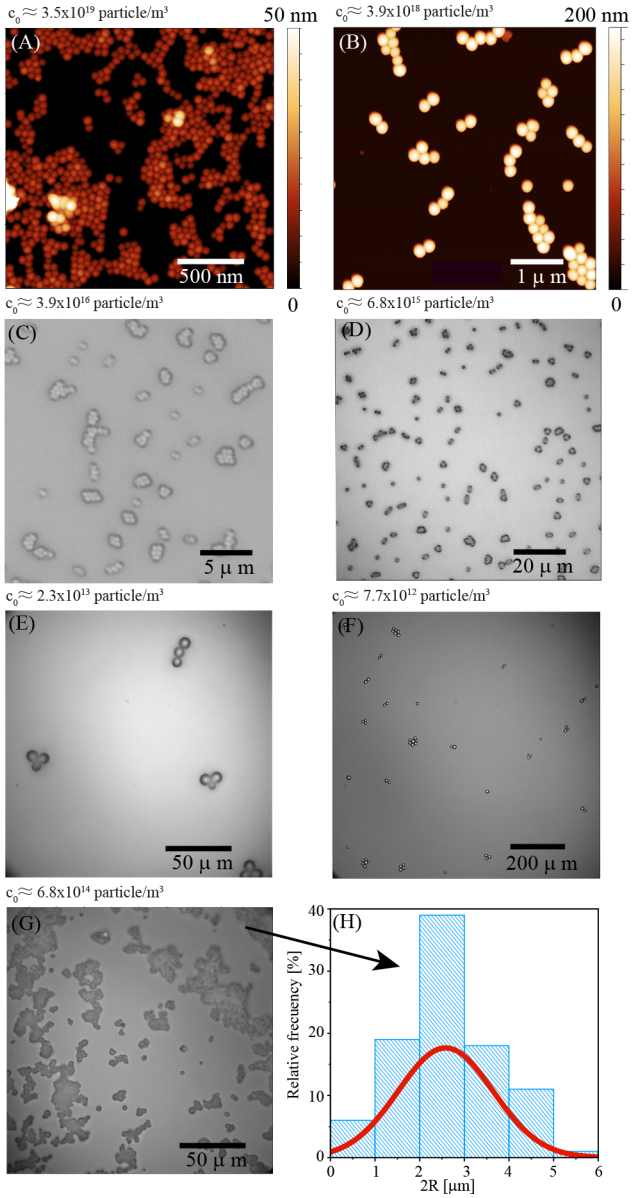

Figure 3. Surface coverage with particles deposited from dispersions of x_0 = 0.01 w/w at ω = 1000 rpm. (A–D) Silica particles (SiO_2) with diameters of d_p = 50, 200, 550, and 1000 nm. (E and F) Polystyrene particles (PS) with d_p = 8 and 25 μm. (G) Calcium carbonate particles ($CaCO_3$) with a mean diameter of d_p = 2.6 μm. (H) Details of the particle size distribution in frame G. The silica particles with d_p = 50 and 200 nm and the PS particles with d_p = 8 μm were dispersed in ethanol. The other particles were dispersed in water.

NP Coverage as a Function of Concentration and Size. Figure 4 shows the number of particles deposited per unit area, Γ, scaled with the transition height, h_{tr}, as a function of the weighing in concentration, c_0 (in number of particles per volume). Data are shown for particles consisting of SiO_2, PS, $CaCO_3$, and Au, with sizes ranging from 50 nm to 25 μm dispersed in water and ethanol. They were deposited at different speeds of 500, 1000, and 3000 rpm. (Only a selection and not all possible combinations of particle sizes, solvents, and speeds were investigated.) The evaporation rates as well as transition heights depend on the solvent and on the rotational speeds. (For the thinning curves and numbers on E and h_{tr}, see the Supporting Information.)

DOI: 10.1021/acs.langmuir.8b03311
Langmuir 2019, 35, 3404–3412

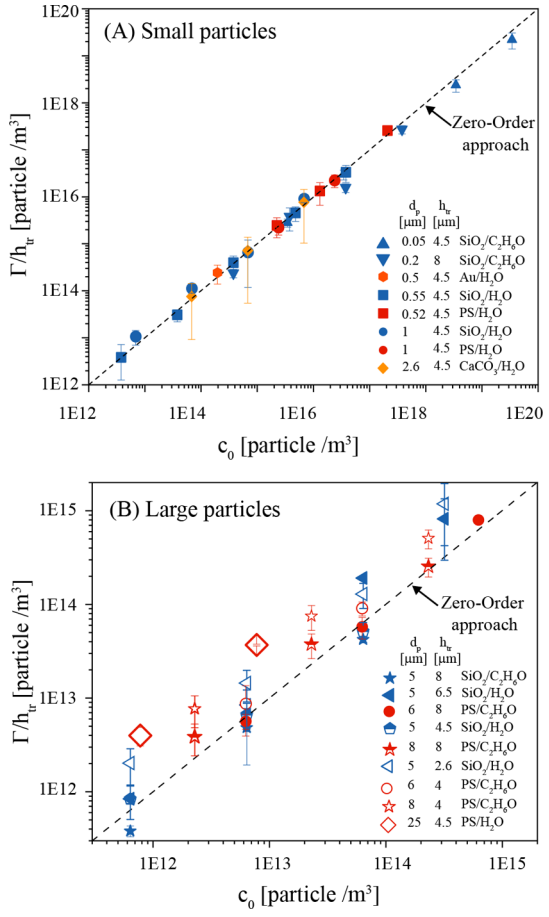

Figure 4. Final coverage Γ (in number of particles per area), scaled by the transition height, h_{tr}, as a function of the initial concentration, c_0 (in number of particles per volume). Data are shown for particles consisting of SiO_2, PS, $CaCO_3$, and Au with sizes ranging from (A) 50 to 2600 nm and from (B) 6000 to 25 000 nm The particles were dispersed in water and ethanol and deposited at different speeds. Shown also are the transition heights h_{tr} in comparison to the particle sizes d_p. The data points are depicted with filled markers for $d_p < h_{tr}$ and with open markers for $d_p > h_{tr}$. (For more technical details, see also the main text and Supporting Information.)

For a meaningful comparison of the observed Γ of these different systems with their different h_{tr} values, in particular for a comparison with the theoretically expected coverages, Γ has been scaled by h_{tr}.[1,2] The dashed line depicts the Γ that is expected from the zeroth-order approach according to eq 5 with constant E and K. Figure 4A shows the data for various different types of (small) particles and the two liquids for particle sizes of up to 2.6 μm in diameter. Figure 4B shows results for (large) particles with diameters of between 5 and 25 μm. Figure 4A reveals that for the smaller particles the observed coverages are in excellent agreement with the coverages predicted by the zeroth-order approach of eq 5. It should be noted that in the case of the $CaCO_3$ particles the error margins are much larger than for the other particles because of the large variation in particle size leading to the somewhat indirect determination of the coverage as described above.

Figure 4B reveals that for the large particles the observed coverage can be significantly larger than what is expected from the zeroth-order approximation. With the rather large number of data points, which in some cases do agree and in some cases do not agree with the zeroth-order behavior, Figure 4B looks rather cluttered. However, there is a clear pattern: If d_p is smaller or about as big as h_{tr}, then the data match the zeroth-order behavior. In the figure, these data points are identified by the filled or half-filled markers. On the other hand, not all particles with $d_p > h_{tr}$ follow the zeroth-order behavior. The coverage of these particles identified by open markers is always higher than expected. There are two exceptions which do not follow this trend: For both concentrations investigated, the 5 μm silica particles dispersed in water and deposited at 500 rpm (filled triangles on the left) are also not in agreement with the zeroth-order behavior, although the particles are smaller than h_{tr}. These observations will be evaluated in more detail in the Discussion section.

Universal Plot of Γ as a Function of Particle Size. Figure 5 shows yet another type of presentation comparing the

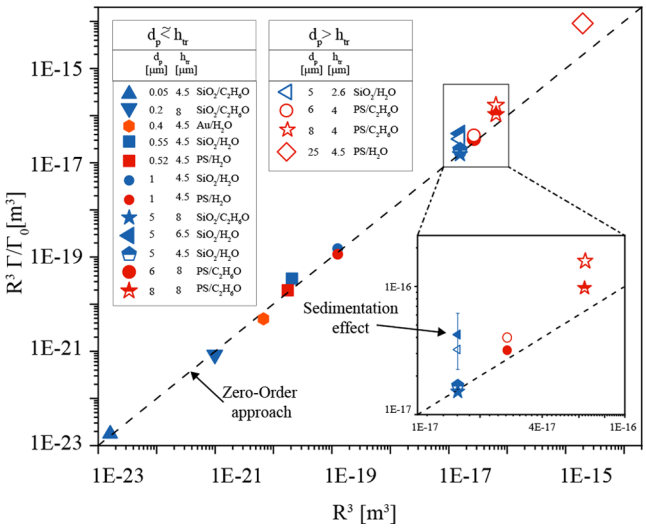

Figure 5. Ratio between the measured coverage (Γ) and the calculated zeroth-order coverage (Γ_0) multiplied by the particle radii cubed, R^3, as a function of the particle radii cubed, R^3. The dashed line indicates $\Gamma = \Gamma_0$. Shown also are the transition heights h_{tr} in comparison to the particle sizes d_p. The data points are depicted with filled markers for $d_p < h_{tr}$ and with open markers for $d_p > h_{tr}$. The inset reveals for which sizes the coverage starts to deviate from the zeroth-order approximation. Indicated also is the case where the deviation can presumably be attributed to sedimentation effects only.

experimentally measured coverages with the coverages expected from the zeroth-order approximation due to eq 5. The data are plotted in a way which explicitly examines the particle size as a key parameter by scaling both axes by the cube of the particle radius. (Please note that this reduces the number of data points because this merges data from different concentrations.) It can be seen that irrespective of the particle material, the solvent, and the rotational speed, the experimental results match the zeroth-order approach quite well if the particles are smaller than h_{tr} (filled or half-filled markers). On the other hand, for d_p much larger than h_{tr} (e.g., for PS particles with $d_p = 25$ μm in H_2O), the coverage clearly does not agree with the zeroth-order behavior. It is much larger than expected (but does not following logarithmic scaling). The deviation from the zeroth-order behavior starts for diameters in the range of or larger than the transition height h_{tr} (open markers). This is highlighted in the inset. This also reveals, as in Figure 4B, the 5 μm silica particles dispersed in water and deposited at 500 rpm as an exception to the general trend.

DOI: 10.1021/acs.langmuir.8b03311
Langmuir 2019, 35, 3404−3412

DISCUSSION

Limits of the Zeroth-Order Approach. *Rheology.* Figure 5 indicates that the approach of calculating the coverage according to eq 5 is correct as long as the particle diameters, d_p, are smaller than h_{tr}. For $d_p > h_{tr}$, the observed coverage is significantly larger than predicted. This may be explained as follows: If the particle diameter is larger than h_{tr}, then the assumption that a film of thickness h_{tr} contains a particle concentration equal to the weighing in concentration is not correct. The zeroth-order scenario assumes that the liquid film containing the dispersed particles is thinning through hydrodynamic (centripedal) flow until it reaches h_{tr}. Supposedly, until the film thickness reaches h_{tr} the particle concentration remains constant because liquid and particles flow radially outward. Around h_{tr}, the hydrodynamic thinning becomes negligible. Evaporation starts to dominate, and the particle concentration increases.

However, with sufficiently large particles (i.e., $d_p > h_{tr}$), this is not correct any more. In this case, as soon as the film thickness h is equal to d_p, *all* particles within a film will contact the substrate. Thus, all particles that are in the film of thickness d_p are more or less immobilized and will finally be deposited. Therefore, in the case of $d_p > h_{tr}$ a rather crude approximation predicts

$$\Gamma_{d_p}(d_p > h_{tr}) \approx c_0 d_p = c_0 \frac{d_p}{h_{tr}} (E/2K)^{1/3} \tag{6}$$

The data in Figure 5 show that for the aqueous dispersion of PS particles with a diameter of $d_p = 25\ \mu m$ the observed coverage Γ is about 5 times larger than what is predicted as Γ_0 (i.e., if the particle size is not taken into account). If $d_p > h_{tr}$, however, is taken into account according to eq 6 (with $h_{tr} \approx 4.5\ \mu m$), then the predicted coverage is ~5- to 6-fold higher. This is in reasonable agreement with the experimental findings.

With the optical microscopy setup, we can directly observe the influence of d_p and h_{tr} on the particle movement and coverage. Figure 6 shows the case of aqueous dispersions (h_{tr} = 4.5 μm) of PS particles with (A) $d_p = 25\ \mu m$ ($x_0 = 6.6 \times 10^{-3}$ w/w) and (B) $d_p = 1\ \mu m$ ($x_0 = 1.3 \times 10^{-4}$ w/w). The images show that in the case of large particles with $d_p = 25\ \mu m \gg h_{tr}$ the number of particles per area decreases as long as $h > d_p$. As soon as $h \approx d_p$, the number of particles per area barely decreases any more. All particles contained in the film of thickness $h \approx d_p$ are finally deposited as described by eq 6. The interference fringes indicate that the film surface is flat for $h > d_p$ and becomes undulated for $h < d_p$. (To account for distortions in the film surface by the menisci created by the particles, h should in this context be defined as the mean volume of liquid per area.) The parallel interference fringes at $h \approx d_p$ show that it is flat but very slightly inclined at $\ll 1°$. In the case of the particles with $d_p = 1\ \mu m \ll h_{tr}$, the particle density decreases as long as $h > h_{tr}$ and remains approximately constant if $h < h_{tr}$. In this case, the final surface coverage is determined by eq 5. (See also movies in the Supporting Information.)

Sedimentation. Figures 5 and 6 and eq 6 indicate that the particle size has a direct influence on the final coverage due to the direct interaction between the hydrodynamic−evaporative film thinnning and the particle concentration. What about the combined impact of particle size and particle density (i.e., sedimentation)? For eqs 5 and 6, it is assumed that the composition within the spreading drop right after deposition and within the layer thinning due to hydrodynamics down to d_p or h_{tr} remains constant and equal to the weighing in value c_0.

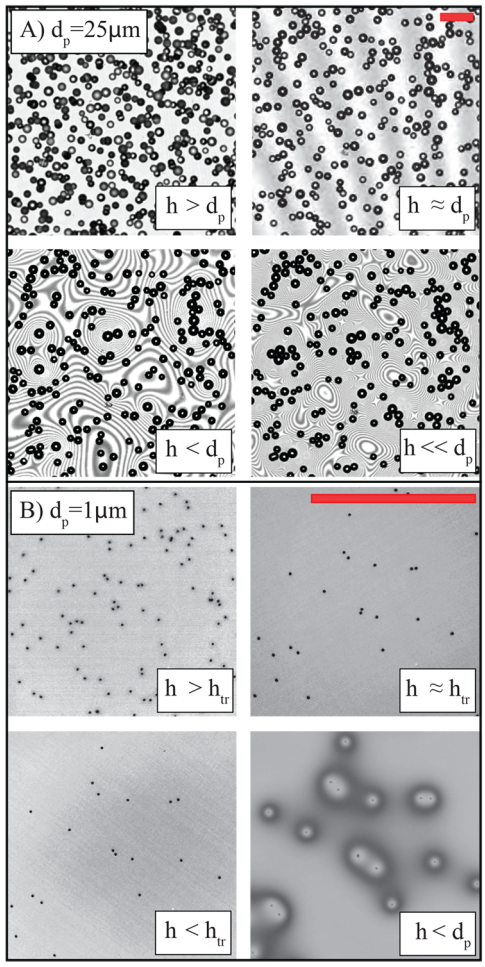

Figure 6. Sequence of optical images recorded during the spin-casting (ω = 1000 rpm, the bar indicates 100 μm) of aqueous dispersions of PS particles with (A) $d_p = 25\ \mu m$ ($x_0 = 6.6 \times 10^{-3}$ w/w) and (B) $d_p = 1\ \mu m$ ($x_0 = 1.3 \times 10^{-4}$ w/w). h = liquid film thickness = mean volume of liquid per area. With the large particles, as long as $h > d_p$, the number of particles per area decreases, and for $h < d_p$, it remains about constant. With the small particles, the number of particles per area decreases as long as $h > h_{tr}$. For $h < h_{tr}$ ($h_{tr} = 4.5 d_p$) and $h < d_p$, it remains constant. In both cases, for $h < d_p$ the liquid surface gets distorted (interference fringes).

With strong sedimentation this may be wrong. As soon as the spin-cast process begins, through sedimentation particles continuously move to the substrate surface and accumulate/attach there. Thus, sedimentation can lead to a final Γ, which is higher than predicted by eq 5. In a rather crude estimation, the extra amount of Γ resulting from sedimentation, $\Gamma_{\overline{\Delta\rho}}$, may be calculated as follows: The speed of sedimentation, $u_{\overline{\Delta\rho}}$, as a function of the relative particle density $\overline{\Delta\rho}$, is given by[31]

$$u_{\overline{\Delta\rho}} = \frac{g}{18\nu} \frac{\rho_p - \rho_L}{\rho_L} d_p^{\,2} = \frac{g}{18\nu} \overline{\Delta\rho} d_p^{\,2} \tag{7}$$

g is the gravitational acceleration (9.8 m s^{-1}), and ν is the kinematic viscosity. Sedimentation leads to a continuous deposition of particles at the substrate surface within a time $t_{\overline{\Delta\rho}}$ of

DOI: 10.1021/acs.langmuir.8b03311
Langmuir 2019, 35, 3404−3412

$$\Gamma_{\overline{\Delta\rho}} = c_0 u_{\overline{\Delta\rho}} t_{\overline{\Delta\rho}} = c_0 \frac{g}{18\nu} \overline{\Delta\rho} d_p^{\,2} t_{\overline{\Delta\rho}} \quad (8)$$

For eq 8, it is assumed that particles reach the substrate and get deposited as they move downward with speed $u_{\overline{\Delta\rho}}$ during time $t_{\overline{\Delta\rho}}$.

In the following text, we assume that the sedimenting particles are smaller than h_{tr}. Therefore, sedimentation accumulates particles during $t_{\overline{\Delta\rho}} = 0.3t_{sc}$ (i.e., the time *before* the film reaches h_{tr} (eq 4)):

$$\Gamma_{\overline{\Delta\rho}} \approx c_0 \frac{\overline{\Delta\rho} g}{18\nu} d_p^{\,2} 0.3 t_{sc} \approx c_0 \frac{\overline{\Delta\rho} g}{18} d_p^{\,2} \frac{1}{2} (2E^2 K)^{-1/3} = c_0 \frac{\overline{\Delta\rho} g}{36\nu E} d_p^{\,2} h_{tr} \quad (9)$$

For a rough estimation, we may assume that sedimentation plays a significant role as soon as it contributes as much to the final coverage as the "regular" deposition process. Thus, eqs 5 and 9 yield

$$c_0 h_{tr} = c_0 \frac{\overline{\Delta\rho} g}{18\nu} d_p^{\,2} \frac{h_{tr}}{2E} \quad (10)$$

This yields a diameter of d_{tr} for the transition between deposition dominated by evaporation and sedimentation:

$$d_{tr} = \sqrt{\frac{36\nu E}{\overline{\Delta\rho} g}} \quad (11)$$

With eq 2, this equation can be written as a function of h_{tr}:

$$d_{tr} = \sqrt{\frac{24\omega^2}{g}} (\overline{\Delta\rho})^{-1/2} h_{tr}^{\,3/2} \quad (12)$$

Equation 12 evaluates the significance of the contribution of sedimentation as a function of $\overline{\Delta\rho}$ and in particular of h_{tr}, the key parameter of any spin-cast process. Let us assume that a dispersion with particles of relative density $\overline{\Delta\rho}$ is spin-cast at a rotational speed ω and with a transition height h_{tr}. Equation 12 says that if the particle diameter is smaller than d_{tr}, then the contributions of sedimentation to Γ can be neglected. If they are larger than d_{tr}, then sedimentation plays a role.

If the particles are smaller than h_{tr} but larger than d_{tr} (i.e., no direct size effect but sedimentation plays a role), as a first approximation, one may combine eqs 5 and 9 and assume

$$\Gamma \approx \Gamma_0 + \Gamma_{\overline{\Delta\rho}}$$

$$\Gamma \approx c_0 h_{tr} + c_0 \frac{\overline{\Delta\rho} g}{18\nu} d_p^{\,2} \frac{h_{tr}}{2E}$$

$$\Gamma \approx c_0 h_{tr} \left[1 + \frac{\overline{\Delta\rho} g}{36\nu E} d_p^{\,2} \right] \quad (13)$$

It is interesting to compare the experimentally measured surface coverages with the estimations based on eq 5 (zeroth-order approach) and its potential limitations due to the particle size ($d_p > h_{tr}$) or sedimentation effects. To this end, the data of equally sized silica particles deposited under different conditions are analyzed. Silica is significantly denser than water. Thus, in contrast to PS, sedimentation may play a role. This may be the reason for the outlier(s) found in Figure 4B and indicated as the "sedimentation effect" in Figure 5. We observe the following:

(1) The data of the 5 μm silica particles dispersed in C_2H_6O and deposited at 1000 rpm (marked with a filled cross) follow the zeroth-order approach. This is in agreement with the absence of a geometrical size effect (eq 6) because the particles are significantly smaller than the transition height (h_{tr} = 8 μm). The speed of sedimentation ($u_{\overline{\Delta\rho}} \approx 14$ μm/s see eq 7), on the other hand, is substantially faster than the evaporation speed (3.2 μm/s). Therefore, according to our rough estimation sedimentation should play a role, which we do not observe.

(2) The 5 μm silica particles dispersed in H_2O and deposited at 3000 rpm (marked with an open triangle pointing to the left) are larger than the transition height (h_{tr} = 2.6 μm). We expect a size effect, and sedimentation should also play a role with $u_{\overline{\Delta\rho}} \approx 14$ μm/s compared to $E \approx 1$ μm/s. We observe that the coverage is in fact substantially higher than expected from the zeroth-order approximation.

(3) The 5 μm silica particles dispersed in H_2O and deposited at 500 rpm (marked with a filled triangle pointing to the left) are smaller than the transition height (h_{tr} = 6.5 μm), so there should be no geometrical size effect. However, the sedimentation speed ($u_{\overline{\Delta\rho}} \approx 14$ μm/s is much larger (30 times) than the speed of evaporation ($E \approx 0.5$ μm/s). We observe a significant deviation from the zeroth-order approximation.

The findings with the PS and the silica particles indicate that the geometrical particle size d_p is important. As soon as $d_p > h_{tr}$, the zeroth-order approach does not work anymore, and the deposited coverage is larger than expected. This is also supported by online imaging investigations, which readily show the size effect. Cases 1 and 3 indicate that the impact of sedimentation appears to be substantially overestimated by the approach of eqs 7−13 Sedimentation may influence the final coverage only if $u_{\overline{\Delta\rho}} >> E$. The reason is not clear. It may be that eqs 7−13 strongly overestimate sedimentation because $u_{\overline{\Delta\rho}}$ is not correct under the given conditions. It is assumed that the sedimentation process relevant to the correction of the deposition occurs in the time before the film reaches h_{tr}. However, during this stage of the spin-cast process, liquid flow flattens the liquid. This flow (stirring) may affect (reduce) the effective sedimentation speed in comparison to $u_{\overline{\Delta\rho}}$ as calculated by eq 7. Nevertheless, the estimation based on eqs 7−13 is still quite valuable because it reveals a lower limit for corrections of the zeroth-order approximation due to sedimentation. It shows, for instance, that the deposition of even rather large (d_p = 0.4 μm) gold nanoparticles with a very high relative density in water ($\overline{\Delta\rho} \approx 18.3$) should not be affected by sedimentation (and of course not by its size with $d_p \ll h_{tr}$). Indeed, the coverage of such particles well matches the zeroth-order assumption (Figures 4 and 5).

Figure 7 sums up the analysis regarding the impact of size and sedimentation on the final coverage. It reveals in an overview plot under which spin-cast conditions the final coverage of particles, Γ, can be described reasonably well by the zeroth-order approximation only (eq 5) or when it needs correction due to size effects (eq 6) and/or sedimentation (eq 13). Figure 7A shows the general relations between the various parameters for ω = 1000 rpm. Figure 7B shows how the plot is used to estimate the deposition behavior of a specific dispersion. Both figures

DOI: 10.1021/acs.langmuir.8b03311
Langmuir 2019, 35, 3404−3412

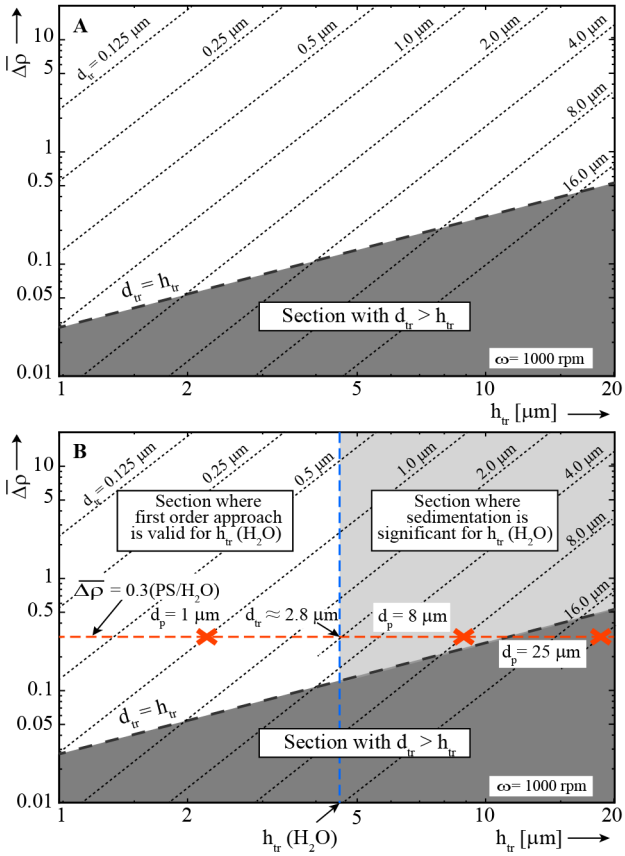

Figure 7. (A) Threshold of the particle size (d_{tr}) deposited from spin-casting, as a function of the relative density $\overline{\Delta\rho}$ and the h_{tr}, in which the fine dashed lines (~40°) calculated with eq 12 for ω = 1000 rpm represent the particle diameter where the film thinning equalizes the sedimentation speed (eq 10) for a given system. On the left side, the sedimentation can be neglected, and for larger particles (to the right of the specific dashed line), it is expected that sedimentation plays a role and deviates from the prediction by excess. The dashed blue line marks the h_{tr} for water; it represents the ultimate limit for eq 5 with respect to the particle size, $d_p = h_{tr}$, where the thick dashed line (~15°) cuts the discontinuous ones. On the left side of the h_{tr} is the working area, and the right side of h_{tr} in eq 5 is no longer valid. (B) The condition of an aqueous dispersion of PS particles is marked with a red dashed line: experimentally tested particle sizes are marked with red crosses over the three plot regions.

show a plot of $\overline{\Delta\rho}$ versus h_{tr}, covering their practically useful ranges. The dashed straight line computed from eq 11, which is inclined at about 15°, is the borderline for the pure size effect. It marks $d_{tr} = h_{tr}$. For spin-cast conditions that are located below this line, the particle size, d_{tr}, is larger than h_{tr}. In this case, the final coverage should be estimated by eq 6. Sedimentation is affected by size and $\overline{\Delta\rho}$, and cases located above the dashed line may or may not be affected by sedimentation. Relevant for an estimation of the contribution from sedimentation are the dotted parallel lines, inclined at about 40° (calculated by eq 11), marking specific particle diameters.

How particle size and specific spin-cast conditions are taken into account is demonstrated with examples of three particles sizes of 1, 8, and 25 μm diameter in Figure 7B (indicated by the red crosses). An aqueous dispersion of PS particles is assumed. This means that the specific conditions are h_{tr} = 4.5 μm (the vertical dashed blue line) and $\overline{\Delta\rho}$ = 0.3 (the horizontal dashed red line). The crossover between these two conditions and the corresponding particle size, d_{tr} (dotted lines), identifies the transition diameter for particles under these conditions. According to Figure 7B, we obtain for this case $d_{tr} \approx 2.8$ μm. This means that for particles which are smaller than 2.8 μm and spin-cast under these conditions, sedimentation can be neglected for the calculation of Γ. If they are larger, then sedimentation may contribute to Γ (with the restrictions discussed above). Hence, for instance, the final coverage for particles with a diameter of 1 μm can be calculated with the zeroth-order approximation (eq 5). For the final coverage of particles with a diameter of 8 μm, on the other hand, sedimentation might be considered (eq 13). For particles with a diameter of 25 μm, the pure size effect (their diameter is larger than h_{tr}) and possibly sedimentation have to be considered. This means also that eq 13 is not correct in this case because the time during which sedimentation may add to Γ is shorter than t_{tr} (because $d_p > h_{tr}$). In this case, one could estimate the contributions of size (eq 13) and sedimentation (eq 6, assuming t_{tr}) separately and chose for a correction of Γ, whatever correction contribution is larger.

It should be noted that the particle sizes of 1 and 25 μm depicted in Figure 7B reflect the real cases presented in the Materials and Methods section (Figure 5). On the other hand, the conditions for the PS particles with d_p = 8 μm presented in Materials and Methods were significantly different. Ethanol, which was used as a liquid instead of water in this case, has a much larger h_{tr} (~7.5 μm). This corresponds to $d_{tr} \approx 6$ μm. Therefore, in this case the contribution from sedimentation to Γ is relatively weak. In fact, Figure 4 shows that Γ for these particles is only slightly larger than what is predicted in the zeroth-order approach.

SUMMARY AND CONCLUSIONS

The deposition of nano- and microsize spherical particles dispersed in volatile liquids is investigated as a function of the weighing in concentration, the particle size, and the densities of liquid and particles. The particles are deposited by hydrodynamic evaporative spin-casting. The deposition process is investigated online optically during the spin-cast process, and the final particle coverage is measured. The data are analyzed in view of the zeroth-order approach. This approach assumes a simple hydrodynamic evaporative behavior of the liquid only, without taking into account any impact of the dispersed particles. It has been used successfully to describe the deposition of monomer and polymer films. For particle dispersions, we find that the zeroth-order approach works quantitatively quite well for particle sizes up to a few micrometers in diameter. For larger particles, the observed final coverage exceeds the predicted value significantly.

We found the causes for this deviation and analyzed them. A theoretical approach is presented, which describes the impact of the particle size and the particle weight on the final particle coverage. It is suggested that large particles have an impact on the transition between hydrodynamic and evaporative film thinning and thus on the outcome of the deposition process. The sedimentation of particles may also contribute to the final coverage if the particle density is significantly larger than the density of the liquid and if the particles are large enough. For both cases of size and sedimentation contributions, we present the threshold conditions which mark the deviations from the zeroth-order description. In addition, we present a new, rather general theoretical approach which takes size and/or sed-

DOI: 10.1021/acs.langmuir.8b03311
Langmuir 2019, 35, 3404−3412

imentation effects into account. This permits the prediction of the final particle coverage even for rather large and/or heavy particles. The predictions seem to quantitatively overestimate the contribution of sedimentation (particle weight contributions), but regarding the particle size effects, the presented corrections to the zeroth-order approximation are in good quantiative agreement with the experimental results. This is quite relevant because it is shown that in most practical cases, if corrections are necessary, corrections due to particle size are more important.

■ ASSOCIATED CONTENT

Supporting Information

The Supporting Information is available free of charge on the ACS Publications website at DOI: 10.1021/acs.langmuir.8b03311.

Thinning curves, spin-casting parameter, deposited particles, and movie descriptions (PDF)

Online thinning of PS particle aqueous dispersions for d_p = 1000 nm (AVI)

Online thinning of PS particle aqueous dispersions for d_p = 25 000 nm (AVI)

■ AUTHOR INFORMATION

Corresponding Authors

*E-mail: JoseAngel.Danglad-Flores@mpikg.mpg.de.
*E-mail: hans.riegler@mpikg.mpg.de.

ORCID

Andre G. Skirtach: 0000-0002-4468-7620
Hans Riegler: 0000-0002-9023-5668

Notes

The authors declare no competing financial interest.

■ ACKNOWLEDGMENTS

We thank Reinhard Lipowsky for institutional support. J.D.-F. was funded by the DAAD and DFG through the IRTG 1524. For assistance with the thinning curve analysis, we thank Stephan Eickelmann, J.D.-F. thanks the GISDE, Universidad de Oriente, Venezuela for his training. We thank Dr. B. V. Parakhonskiy for assistance with particle preparation, and A.G.S. acknowledges the support of BOF (UGent) and FWO (Flanders Research Council).

■ REFERENCES

(1) Karpitschka, S.; Weber, C. M.; Riegler, H. Spin casting of dilute solutions: Vertical composition profile during hydrodynamic-evaporative film thinning. *Chem. Eng. Sci.* **2015**, *129*, 243−248.

(2) Danglad-Flores, J.; Eickelmann, S.; Riegler, H. Deposition of polymer films by spin casting: A quantitative analysis. *Chem. Eng. Sci.* **2018**, *179*, 257−264.

(3) Larson, R. G.; Rehg, T. J. In *Liquid Film Coating: Scientific Principles and Their Technological Implications*; Kistler, S. F., Schweizer, P. M., Eds.; Springer: Dordrecht, The Netherlands, 1997; pp 709−734.

(4) Darling, S. B.; Yufa, N. A.; Cisse, A. L.; Bader, S. D.; Sibener, S. J. Self-Organization of FePt Nanoparticles on Photochemically Modified Diblock Copolymer Templates. *Adv. Mater.* **2005**, *17*, 2446−2450.

(5) Sun, J.; Li, Z.; Sun, Y.; Zhong, L.; Huang, J.; Zhang, J.; Liang, Z.; Chen, J.; Jiang, L. Uniform and reproducible plasmon-enhanced fluorescence substrate based on PMMA-coated, large-area Au@ Ag nanorod arrays. *Nano Res.* **2018**, *11*, 953−965.

(6) Shojaeiarani, J.; Bajwa, D. S.; Stark, N. M. Spin-coating: A new approach for improving dispersion of cellulose nanocrystals and mechanical properties of poly (lactic acid) composites. *Carbohydr. Polym.* **2018**, *190*, 139−147.

(7) Tans, S. J.; Devoret, M. H.; Dai, H.; Thess, A.; Smalley, R. E.; Geerligs, L.; Dekker, C. Individual single-wall carbon nanotubes as quantum wires. *Nature* **1997**, *386*, 474.

(8) Johnston-Peck, A. C.; Wang, J.; Tracy, J. B. Formation and grain analysis of spin-cast magnetic nanoparticle monolayers. *Langmuir* **2011**, *27*, 5040−5046.

(9) Coe-Sullivan, S.; Steckel, J. S.; Woo, W.-K.; Bawendi, M. G.; Bulović, V. Large-Area Ordered Quantum-Dot Monolayers via Phase Separation During Spin-Casting. *Adv. Funct. Mater.* **2005**, *15*, 1117−1124.

(10) Jiang, P.; Prasad, T.; McFarland, M. J.; Colvin, V. L. Two-dimensional nonclose-packed colloidal crystals formed by spincoating. *Appl. Phys. Lett.* **2006**, *89*, 011908.

(11) Jiang, P.; McFarland, M. J. Large-scale fabrication of wafer-size colloidal crystals, macroporous polymers and nanocomposites by spin-coating. *J. Am. Chem. Soc.* **2004**, *126*, 13778−13786.

(12) Wang, D.; Möhwald, H. Rapid fabrication of binary colloidal crystals by stepwise spin-coating. *Adv. Mater.* **2004**, *16*, 244−247.

(13) Toolan, D. T.; Fujii, S.; Ebbens, S. J.; Nakamura, Y.; Howse, J. R. On the mechanisms of colloidal self-assembly during spin-coating. *Soft Matter* **2014**, *10*, 8804−8812.

(14) DeSilva, L. A.; Gadipalli, R.; Donato, A.; Bandara, T. Reflectivity of 88% for four-period hybrid Bragg mirror from spin coating process. *Optik* **2018**, *157*, 360−364.

(15) DeSilva, L. A.; Thakurdesai, M.; Bandara, T. M. W. J.; Preston, J.; Johnson, W.; Gaquere-Parker, A.; Survase, S. Synthesis of dense TiO2 nanoparticle multilayers using spin coating technique. *Appl. Phys. A: Mater. Sci. Process.* **2018**, *124*, 314.

(16) Hong, Y.-K.; Kim, H.; Lee, G.; Kim, W.; Park, J.-I.; Cheon, J.; Koo, J.-Y. Controlled two-dimensional distribution of nanoparticles by spin-coating method. *Appl. Phys. Lett.* **2002**, *80*, 844−846.

(17) Meyerhofer, D. Characteristics of resist films produced by spinning. *J. Appl. Phys.* **1978**, *49*, 3993−3997.

(18) Bornside, D.; Macosko, C.; Scriven, L. Spin coating: One-dimensional model. *J. Appl. Phys.* **1989**, *66*, 5185−5193.

(19) Bornside, D.; Macosko, C.; Scriven, L. Spin coating of a PMMA/chlorobenzene solution. *J. Electrochem. Soc.* **1991**, *138*, 317−320.

(20) Reisfeld, B.; Bankoff, S.; Davis, S. The dynamics and stability of thin liquid films during spin coating. I. Films with constant rates of evaporation or absorption. *J. Appl. Phys.* **1991**, *70*, 5258−5266.

(21) Reisfeld, B.; Bankoff, S.; Davis, S. The dynamics and stability of thin liquid films during spin coating. II. Films with unit-order and large Peclet numbers. *J. Appl. Phys.* **1991**, *70*, 5267−5277.

(22) Bornside, D. E.; Brown, R. A.; Ackmann, P. W.; Frank, J. R.; Tryba, A. A.; Geyling, F. T. The effects of gas phase convection on mass transfer in spin coating. *J. Appl. Phys.* **1993**, *73*, 585−600.

(23) Cregan, V.; O'Brien, S. A note on spin-coating with small evaporation. *J. Colloid Interface Sci.* **2007**, *314*, 324−328.

(24) Emslie, A. G.; Bonner, F. T.; Peck, L. G. Flow of a viscous liquid on a rotating disk. *J. Appl. Phys.* **1958**, *29*, 858−862.

(25) Haas, D. E.; Quijada, J. N.; Picone, S. J.; Birnie, D. P. Effect of solvent evaporation rate on skin formation during spin coating of complex solutions. *Proc. SPIE* **2000**, *3943*, 280−284.

(26) Volodkin, D. V.; Petrov, A. I.; Prevot, M.; Sukhorukov, G. B. Matrix polyelectrolyte microcapsules: new system for macromolecule encapsulation. *Langmuir* **2004**, *20*, 3398−3406.

(27) Eickelmann, S.; Riegler, H. Rupture of ultrathin solution films on planar solid substrates induced by solute crystallization. *J. Colloid Interface Sci.* **2018**, *528*, 63−69.

(28) Köhler, R.; Lazar, P.; Riegler, H. Optical imaging of thin films with molecular depth resolution. *Appl. Phys. Lett.* **2006**, *89*, 241906.

(29) Eickelmann, S.; Danglad-Flores, J.; Chen, G.; Miettinen, M. S.; Riegler, H. Meniscus Shape around Nanoparticles Embedded in Molecularly Thin Liquid Films. *Langmuir* **2018**, *34*, 11364.

(30) Peurrung, L.; Graves, D. Film thickness profiles over topography in spin coating. *J. Electrochem. Soc.* **1991**, *138*, 2115−2124.

DOI: 10.1021/acs.langmuir.8b03311
Langmuir 2019, 35, 3404−3412

(31) Davis, R. H.; Acrivos, A. Sedimentation of noncolloidal particles at low Reynolds numbers. *Annu. Rev. Fluid Mech.* **1985**, *17*, 91−118.

DOI: 10.1021/acs.langmuir.8b03311
Langmuir 2019, 35, 3404−3412